npj | computational materials

Article

Published in partnership with the Shanghai Institute of Ceramics of the Chinese Academy of Sciences

https://doi.org/10.1038/s41524-024-01362-y

High temperature ferrimagnetic semiconductors by spin-dependent doping in high temperature antiferromagnets

Jia-Wen Li [1], Gang Su [1,2,3,4] ✉ & Bo Gu [1,2,3] ✉

To realize room temperature ferromagnetic (FM) semiconductors is still a challenge in spintronics. Many antiferromagnetic (AFM) insulators and semiconductors with high Neel temperature T_N are obtained in experiments, such as $LaFeO_3$, $BiFeO_3$, etc. High concentrations of magnetic impurities can be doped into these AFM materials, but AFM state with very tiny net magnetic moments was obtained in experiments because the magnetic impurities were equally doped into the spin up and down sublattices of the AFM materials. Here, we propose that the effective magnetic field provided by a FM substrate could guarantee the spin-dependent doping in AFM materials, where the doped magnetic impurities prefer one sublattice of spins, and the ferrimagnetic (FIM) materials are obtained. To demonstrate this proposal, we study the Mn-doped AFM insulator $LaFeO_3$ with FM substrate of Fe metal by the density functional theory (DFT) calculations. It is shown that the doped magnetic Mn impurities prefer to occupy one sublattice of the AFM insulator and introduce large magnetic moments in La(Fe, Mn)O_3. For the AFM insulator $LaFeO_3$ with high $T_N = 740$ K, several FIM semiconductors with high Curie temperature $T_C > 300$ K and the band gap less than 2 eV are obtained by DFT calculations when 1/8 or 1/4 Fe atoms in $LaFeO_3$ are replaced by the other 3d, 4d transition metal elements. The large magneto-optical Kerr effect (MOKE) is obtained in these $LaFeO_3$-based FIM semiconductors. In addition, the FIM semiconductors with high T_C are also obtained by spin-dependent doping in some other AFM materials with high T_N, including $BiFeO_3$, $SrTcO_3$, $CaTcO_3$, etc. Our theoretical results propose a way to obtain high T_C FIM semiconductors by spin-dependent doping in high T_N AFM insulators and semiconductors.

In spintronics, it is still a challenge in experiments to realize room temperature ferromagnetic (FM) semiconductors. The Curie temperature T_C of intrinsic two- and three-dimensional FM semiconductors are still far below the room temperature[1–9], which largely limit their applications.

Doping is an effective approach to control the physical properties of materials. By doping a small amount of magnetic impurities into non-magnetic semiconductors, the magnetic properties of the materials can be dramatically improved, these materials are called dilute magnetic semiconductors (DMS)[10–17]. For the classic DMS (Ga, Mn)As its highest T_C can reach 200 K[18]. High T_C DMSs have been reported in recent experiments, such as $T_C = 230$ K in (Ba, K)(Zn, Mn)$_2As_2$ with 15% doping of Mn[19,20], $T_C = 340$ K in (Ga, Fe)Sb with 25% doping of Fe[21], $T_C = 385$ K in (In, Fe)Sb with 35% doping of Fe[22], $T_C = 280$ K in ($Si_{0.25}Ge_{0.75}$, Mn) with 5% doping of Mn[23], etc.

In contrast to DMS, there are also some studies on the magnetic impurities doped antiferromagnetic (AFM) insulators and semiconductors in experiments. Some AFM insulators and semiconductors with high Neel temperature T_N have been obtained experimentally, as shown in Table 1[24–39]. Being a high T_N AFM insulator, $LaFeO_3$ has attracted a lot of attention due to its interesting properties. $LaFeO_3$ has a perovskite structure with chemical

[1]Kavli Institute for Theoretical Sciences, University of Chinese Academy of Sciences, Beijng, China. [2]CAS Center for Excellence in Topological Quantum Computation, University of Chinese Academy of Sciences, Beijng, China. [3]Physical Science Laboratory, Huairou National Comprehensive Science Center, Beijing, China. [4]School of Physical Sciences, University of Chinese Academy of Sciences, Beijng, China. ✉e-mail: gsu@ucas.ac.cn; gubo@ucas.ac.cn

formula of ABO_3[24–26]. A high $T_N = 740$ K has been observed in $LaFeO_3$[26], where the magnetic ground state is G-AFM with intralayer and interlayer AFM order. $LaFeO_3$ has a large optical band gap of 2.05–2.51 eV in experiments[27,40]. Room temperature ferroelectricity of $LaFeO_3$ has also been observed[41]. In addition, the doped $LaFeO_3$ has also been studied, such as (La, X)FeO_3 with x = Sr[42], Al[43], Bi[44,45], Ca[46], Ba[46], and La(Fe, D)O_3 with D = Mo[47], Ni[48], Cr[49–52], Ti[40,53,54], Zn[27,55], Cu[56], Mn[57], Mg[58], Co[59], etc. It shows a high tolerance to impurities, the doping concentration at both La and Fe sites could reach to about 50%. Some magnetic impurities doped AFM insulators and semiconductors with high T_N are shown in Table 2. The experimental studies of La($Fe_{1-x}D_x$)O_3[27,40,47–57], Bi($Fe_{1-x}D_x$)O_3[60–65], and ($Ni_{1-x}D_x$)O[66–69] have shown very tiny net magnetic moments, although the high concentrations of magnetic impurities can be realized.

Table 1 | Some antiferromagnetic (AFM) insulators and semiconductors with high Neel temperatrue T_N in experiments

AFM materials	T_N (K)	Gap (eV)	Experiments
$LaFeO_3$	740	2.5	Ref. 24–27
$BiFeO_3$	640	2.5	Ref. 28
$SrTcO_3$	1023	1.5	Ref. 29
$CaTcO_3$	850	2.2	Ref. 30
NiO	525	3.2	Ref. 31,32
LaOMnP	375	1.4	Ref. 33
LaOMnAs	317	0.4	Ref. 34,35
MnTe	307	1.4	Ref. 36
LiMnAs	374	0.2	Ref. 34,37
Cr_2O_3	340	3.3	Ref. 38,39

As shown in Table 2, there is an increase of net magnetic moment in AFM materials after doping, which was explained as the formation of clusters[49,50,52,55], enhancement of interface effects[40,52,53], change of magnetic coupling[50–52,56], etc. However, their net magnetic moment is still negligible, which can be understood from the symmetry of spin up and down sublattices of AFM host materials. As shown in Fig. 1, magnetic impurities were equally doped into the spin up and down sublattices of the AFM materials, resulting in zero net magnetic moment. On the other hand, as shown in Table 2, only a few theoretical studies focus on the magnetic impurities doped AFM insulators and semiconductors, and nearly have not discussed the theoretical results of magnetic properties, such as T_N[70–75]. Is there a way to break the symmetry of spin up and down sublattices of AFM host materials?

In this paper, we propose that the effective magnetic field from the FM substrate can break the symmetry of spin up and down sublattices and make spin-dependent doping possible in AFM materials, as schematically shown in Fig. 1. To demonstrate our proposal, we study the Mn-doped AFM insulator $LaFeO_3$ with FM substrate of Fe metal by the density functional theory (DFT) calculations. The calculation results for the supercell La(Fe, Mn)O_3/bcc-Fe show that the doped magnetic Mn impurities prefer to occupy one sublattice of AFM insulator, and introduce large magnetic moments in La(Fe, Mn)O_3. By this way, some ferrimagnetic (FIM)

Table 2 | Some magnetic impurities doped AFM insulators and semiconductors with high T_N

Materials	Properties	D	Experiments					Theories		
			x	$\langle M \rangle$	T_N	Gap	Ref	x	Gap	Ref
	$La(Fe_{1-x}D_x)O_3$	Mo	0.25	1×10^{-2}	RT	y	47			
		Zn	0.30	1×10^{-4}			27,55			
		Ti	0.20	2×10^{-3}			40,53,54			
		Ni	0.30	1×10^{-2}			48			
		Cu	0.20	/			56			
		Cr	0.50	1×10^{-3}			49–52	0.5	n	70
		Mg	0.30	/			58			
		Co	0.10				59			
		Nb						0.25	n	71
		V						0.25	y	72
	$Bi(Fe_{1-x}D_x)O_3$	Co	0.30	5×10^{-2}	RT	y	61,62,64	0.125	y	73
		Mn	0.20	/			60	0.125		73
		Cr, Ni, V	0.03	1×10^{-3}			64	0.125		73
		Nb	0.01	1×10^{-3}			63			
		Y	0.10	/			65			
		Cu, Zn						0.25	y	74
	$(Ni_{1-x}D_x)O$	Zn	0.05	1×10^{-4}	RT	y	66			
		Fe	0.02	1×10^{-4}			67			
		Mn	0.06	1×10^{-3}			68			
		Nd	0.03	1×10^{-4}			69			
		Li, Cu, Ag						0.083	y	75
	$(Mn_{1-x}D_x)Te$	Cu	0.075	/	RT	/	96			
		Cr	0.05	3×10^{-2}	280 K		97			
	$Sr(Tc_{1-x}D_x)O_3$	Ru	0.75	4×10^{-2}	150 K		98			

x is the doping concentration. $\langle M \rangle$ is the average magnetic moment per magnetic atom in unit of μ_B. RT means T_N is above room temperature, and y and n denotes yes and no, respectively. In addition, / denote that the related property is not discussed in the references.

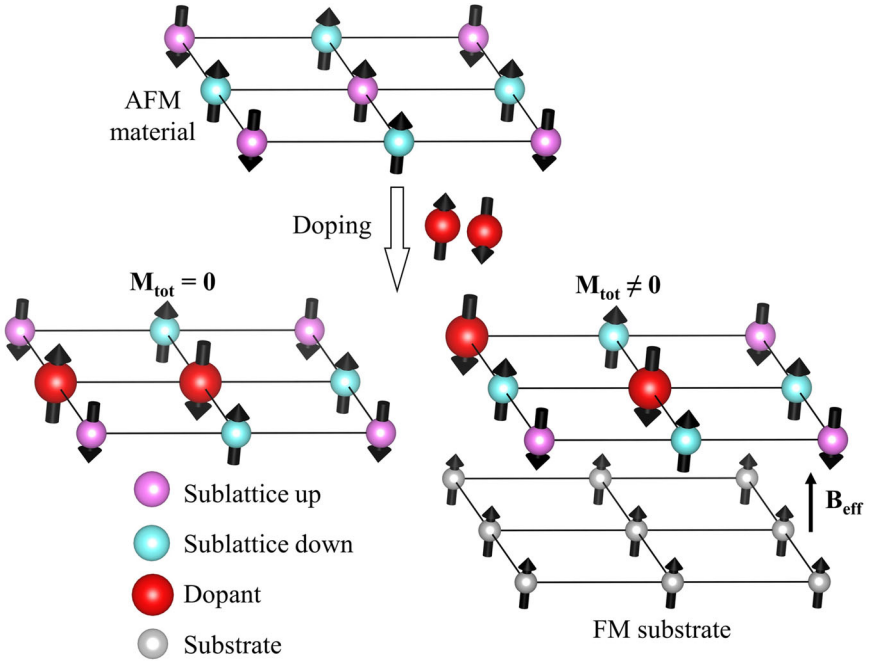

Fig. 1 | Schematic diagram of spin-independent doping (left) with zero net magnetic moment and spin-dependent doping (right) with non-zero net magnetic moment, for the antiferromagnetic (AFM) materials doped with magnetic impurities.

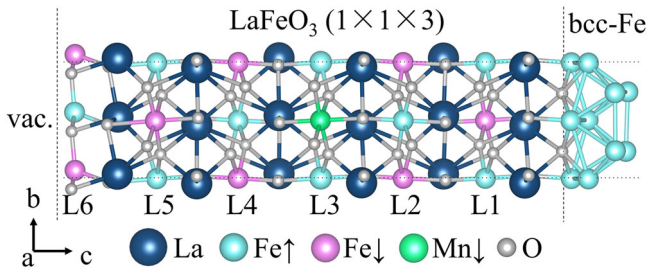

Fig. 2 | Crystal structure of the supercell La(Fe, Mn)O_3/bcc-Fe, where the Mn impurity are doped at Fe site of layer L3.

semiconductors with Curie temperature T_C above room temperature are predicted for $La(Fe_{1-x}D_x)O_3$ with D = 3d, 4d transition metal impurities and $x = 0.125$ and 0.25. In addition, $La(Fe_{0.75}D_{0.25})O_3$ shows large magneto-optical Kerr effect. The variation of T_C in the FIM $La(Fe_{1-x}D_x)O_3$ as a function of elements D can be well understood by a formula of mean-field theory. Our results propose a way to obtain high-temperature FIM semiconductors by spin-dependent doping in high-temperature AFM insulators and semiconductors.

Results

Spin-dependent doping

$LaFeO_3$ has a G-AFM ground state and shows very weak ferromagnetism due to the spin canting caused by the Dzyaloshinskii-Moriya (DM) interaction[76]. The net magnetic moment per Fe atom in $LaFeO_3$ is about $10^{-4}\,\mu_B$. Experiments found that doping at Fe sites will increase the net magnetic moment to 10^{-4}~$10^{-2}\,\mu_B$ per Fe atom, while it's still in the G-AFM state, as shown in Table 2. The thin films of $LaFeO_3$ maintain the AFM properties in experiments[77–80].

To break the symmetry of spin up and down sublattices in $LaFeO_3$, we study the AFM insulator $LaFeO_3$ with FM substrate of Fe metal and consider a $LaFeO_3$/bcc-Fe heterojunction, as shown in Fig. 2. The lattice constant is $a = 2.87$ Å for bcc-Fe, and $a = 5.60$ Å, $b = 5.66$ Å for $LaFeO_3$. The lattice of $2 \times 2 \times 1$ bcc-Fe and $LaFeO_3$ fit well with a small lattice mismatch about 1%. The optimized lattice constants of $LaFeO_3$/bcc-Fe heterojunction are $a = b = 5.56$ Å, where three layers of $LaFeO_3$, one layer of bcc-Fe along (001) direction, and a vacuum layer of 20 Å are considered. For simplicity, we fix the spin of the bcc-Fe substrate as spin up.

It is both structural and electronic for the preferential doping sites. As shown in Fig. 2, there are six Fe layers in the $1 \times 1 \times 3$ $LaFeO_3$ supercell, labeled as L1~L6. For each layer, there are both spin up and down sites. As an example, the supercell of La(Fe, Mn)O_3/bcc-Fe with Mn at Layer 3 and spin down sublattice is shown in Fig. 2. The differences of total energy of the supercells La(Fe, D)O_3/bcc-Fe with dopants D = 3d and 4d transition metals at layer α and spin up and down sublattices are calculated as shown in Table 3. There are significant energy differences with dopants D at layer α and spin up and down sublattices, indicating the stability of the spin-dependent doping.

The energy difference of the supercells La(Fe, Mn)O_3/bcc-Fe with Mn at spin up and down sublattices is still significant when impurities Mn are doped at layer 4, i.e., 1.6 nm to the interface. Since the $LaFeO_3$ nanosheets could be as thin as 5 nm[81,82], the influence of Fe substrate is effective. The spin-dependent doping will lead to spin polarization of dopants and induce AFM-FIM transition. Experiment found that the magnetic field will significantly increase the net magnetic moment of ZnO doped with 2% Cr[83].

To study the formation energy of La(Fe, Mn)O_3 with Fe substrate, as shown in Fig. 2, the supercell $La_{12}Fe_{19}MnO_{36}$ is used. The formation energy is calculated by $E_{formation} = (E_{La(Fe,Mn)O_3/bcc-Fe} - 12E_{La} - 19E_{Fe} - E_{Mn} - 36E_O)/68$, where $E_{La(Fe,Mn)O_3/bcc-Fe}$ is energy of supercell La(Fe, Mn)O_3/bcc-Fe with one dopant Mn at layer α and sublattice spin σ. E_{La}, E_{Fe}, and E_{Mn} are energies per atom for bulks of La, Fe, and Mn with symmetries of $P6_3/mmc$, $Im\bar{3}m$ and $I\bar{4}3m$, respectively. E_O is energy per atom for O_2 gas with symmetry C2/m. The formation energies for La(Fe, D)O_3/bcc-Fe with dopants D = 3d and 4d transition metals are calculated in the same way, and the results are shown in Table 3. For dopants D = 3d and 4d transition metals, the obtained formation energies are negative, and lower than the formation energy of −2.435 eV atom^{-1} for host material $LaFeO_3$/bcc-Fe, indicating the stability of doping. In addition, the difference of total energy of the supercells La(Fe, D)O_3/bcc-Fe with dopants D at layer α and spin up and down sublattices is also shown in Table 3. There are significant energy differences with dopants D at spin up and down sublattices, indicating the stability of spin-dependent doping.

The average magnetic moment of Fe atoms in bulk bcc-Fe is 2.95 μ_B. For the supercell La(Fe, Mn)O_3/bcc-Fe with Mn at L3 and spin down sublattice, as shown in Fig. 2, there are two Fe layers in bcc-Fe. The average

Table 3 | Total energy difference and formation energy $E_{formation}$ of the supercells La(Fe, D)O_3/bcc-Fe with dopants D at layer α and sublattice spin σ

Dopants	Position	Distance to interface (nm)	Ground state	$E_{formation(\uparrow)}$ (eV atom^{-1})	$E_{formation(\downarrow)}$ (eV atom^{-1})	$E_{total}(\uparrow) - E_{total}(\downarrow)$ (meV)
Mn	L2	0.8	FIM	−2.483	−2.484	64.1
	L3	1.2		−2.482	−2.483	53.1
	L4	1.6		−2.482	−2.484	88.6
Ti	L2	0.8		−2.533	−2.539	409.0
V				−2.515	−2.517	145.8
Cr				−2.523	−2.522	−72.2
Co				−2.460	−2.429	−2095.3
Ni				−2.459	−2.457	−138.2
Cu				−2.438	−2.438	−22.9
Zr				−2.527	−2.519	−508.0
Nb				−2.543	−2.555	835.2
Mo				−2.481	−2.521	2682.3
Tc				−2.474	−2.463	−766.1
Ru				−2.442	−2.485	2951.8
Rh				−2.480	−2.480	9.8
Pd				−2.440	−2.444	286.6

Layers L2 to L4 are defined in Fig. 6. The formation energy of the host material $LaFeO_3$/bcc-Fe is −2.435 eV atom^{-1}.

magnetic moment is 3.37 μ_B for Fe at the interface and 3.12 μ_B for Fe at the layer next to the interface. Thus, the magnetic moment of Fe substrate near the interface has been slightly enhanced.

T_C in $LaFeO_3$-based FIM semiconductors

The band structure of $LaFeO_3$ is shown in Fig. 3a, with a band gap of 2.38 eV, consistent with the experimental value of 2.05~2.51 eV[27,40]. Since $LaFeO_3$ is AFM with zero net magnetic moment, we determine its T_N through energy and specific heat by Monte Carlo simulations. The results are shown in Fig. 3c, with a sharp peak of specific heat at $T_N = 650$ K, close to the experimental value of 740 K[26].

For the $La(Fe_{0.75}Mn_{0.25})O_3$ where one of the four Fe atoms is replaced by a Mn atom in a $LaFeO_3$ unit cell. DFT results show that its magnetic ground state is FIM. Mn has a magnetic moment of 3.73 μ_B, smaller than Fe (4.18 μ_B), induces a net magnetic moment near 0.12 μ_B per $LaFeO_3$ unit cell. In addition, $La(Fe_{0.75}Mn_{0.25})O_3$ is a FIM semiconductor with a band gap of 0.56 eV, and a high Curie temperature $T_C = 603$ K is estimated by the Monte Carlo simulation, as shown in Fig. 3d.

To study the formation energy of $La(Fe_{0.75}Mn_{0.25})O_3$ without Fe substrate, the unit cell $La_4Fe_3MnO_{12}$ is used. The formation energies are calculated by $E_{formation} = (E_{La(Fe,Mn)O_3} - 4E_{La} - 3E_{Fe} - E_{Mn} - 12E_O)/20$, where $E_{La(Fe,Mn)O_3}$ is the energy of $La_4Fe_3MnO_{12}$ with one dopant Mn at a $LaFeO_3$ unit cell without substrate. The formation energies for La(Fe, D)O_3 with dopants D = 3d and 4d transition metals are calculated in the same way, and the results are shown in Table 4. For dopants D = Sc, Ti, V, Cr, Y, Zr, Nb, Mo, Tc, the obtained formation energies are negative, and lower than the formation energy of −2.71 eV atom^{-1} for host material $LaFeO_3$, indicating the stability of doping. It is noted that without Fe substrate, the formation energies for D at spin up and down sublattices are the same.

In addition, the formation energies of Bi(Fe, D)O_3, Sr(Tc, D)O_3, and Ca(Tc, D)O_3 are calculated in the same way, and the results are shown in Supplementary Tables 4–6 in Supplementary Material, respectively. All the obtained formation energies are negative, and some are lower than the formation energy of the host materials, indicates their stability of doping.

With different 3d and 4d dopants, the magnetic ground states of $La(Fe_{0.75}D_{0.25})O_3$ maintain FIM. Because the magnetic moments of Fe are almost constant compared with different dopants, the net magnetic moment are from the broken of the symmetry of the AFM spin sublattices, which can be calculated as $M_{tot} = |M_{dopant} - M_{Fe}|$, the detailed magnetic moments see Supplementary Table 1 in Supplementary Material. The average magnetic moment per lattice $\langle M \rangle$ of $La(Fe_{0.75}D_{0.25})O_3$ is defined as $\langle M \rangle = M_{tot}/N$, the magnetic lattice number $N = 4$ for the $LaFeO_3$ unit cell, and the results are shown in Fig. 4a. The Curie temperature T_C of $La(Fe_{0.75}D_{0.25})O_3$ which was estimated by the Monte Carlo simulations, as shown in Fig. 4b. It is noted that most of T_C with 3d and 4d dopants are above room temperature.

The band structure of bulk $LaFeO_3$ show spin splitting in k paths $\Gamma - R_2$ and $\Gamma - U_2$. The spin splitting without spin-orbit coupling (SOC) that happens in antiferromagnetic (AFM) materials requires broken θIT and UT symmetry, where θ, I, T, U are the time inverse, space inverse, translation, and spin inverse operations, respectively[84–86]. The crystal space group and magnetic space group of G-AFM $LaFeO_3$ are *pnma* and $P2_1/c$, respectively, allow the spin splitting without soc in part of Brillouin zone[85]. The spin splitting in AFM materials could be k-dependent, according to the symmetry of k space[84]. Similar band structures with k-dependent band splitting in $LaFeO_3$ is obtained and discussed in the previous study[87].

To discuss the effect of concentrations, the material $La(Fe_{0.875}D_{0.125})O_3$ is studied. A $2 \times 1 \times 1$ supercell is considered, where one of eight Fe atoms is replaced by the D (3d or 4d) atom. DFT results show that its magnetic ground state maintain FIM with different dopants. The $\langle M \rangle$ of $La(Fe_{0.875}D_{0.125})O_3$ is about half to that of $La(Fe_{0.75}D_{0.25})O_3$, as shown in Fig. 4c. It is expected since the concentration of dopants decreases from 1/4 to 1/8. It is interesting to note that the T_C of $La(Fe_{0.875}D_{0.125})O_3$ are higher than that of $La(Fe_{0.75}D_{0.25})O_3$, as shown in Fig. 4d.

The calculated values of average magnetic moment per lattice $\langle M \rangle$, Curie temperature T_C, and band gap of $La(Fe_{0.75}D_{0.25})O_3$ and $La(Fe_{0.875}D_{0.125})O_3$ are summarized in Table 4.

MOKE in $LaFeO_3$-based FIM semiconductors

We investigated the magneto-optical Kerr effect for $La(Fe_{0.75}D_{0.25})O_3$. The Kerr rotation angle is given by:

$$\theta_K(\omega) = Re\frac{\varepsilon_{xy}}{(1-\varepsilon_{xx})\sqrt{\varepsilon_{xx}}}, \quad (1)$$

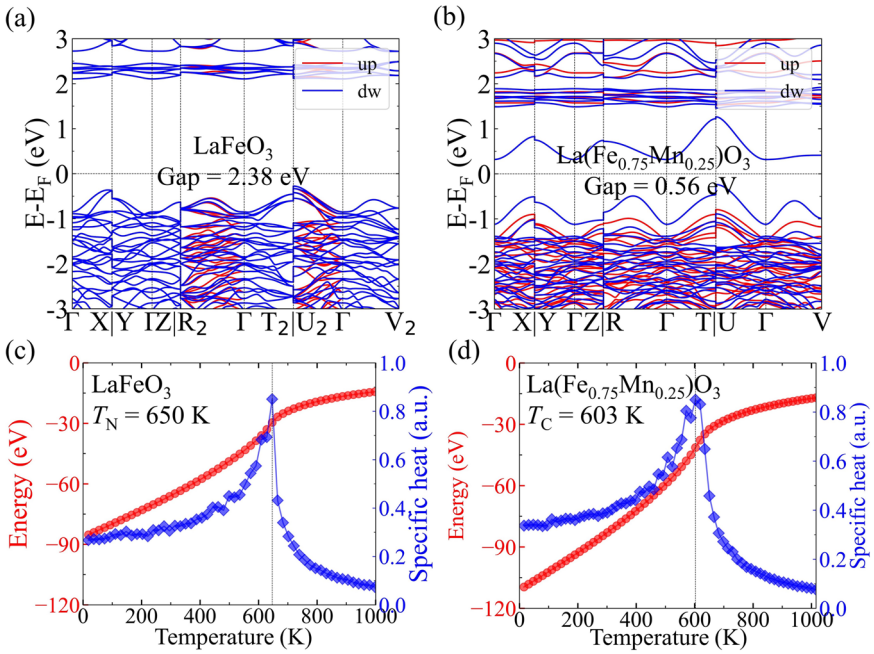

Fig. 3 | Band structures and Monte Calor results of $LaFeO_3$ and $La(Fe_{0.75}Mn_{0.25})O_3$. DFT results of band structure for **a** $LaFeO_3$ with a band gap of 2.38 eV and **b** $La(Fe_{0.75}Mn_{0.25})O_3$ with a band gap of 0.56 eV. Monte Carlo results of energy and specific heat as a function of temperature for **c** $LaFeO_3$ with Neel temperature $T_N = 650$ K and **d** $La(Fe_{0.75}Mn_{0.25})O_3$ with Curie temperature $T_C = 603$ K. Results here are obtained without Fe substrate.

Table 4 | The calculated results of the average magnetic moment per magnetic atom $\langle M \rangle$, band gap, formation energy $E_{formation}$, and Curie temperature T_C for $La(Fe_{0.75}D_{0.25})O_3$ and $La(Fe_{0.875}D_{0.125})O_3$

Dopants	Properties	$La(Fe_{0.75}D_{0.25})O_3$				$La(Fe_{0.875}D_{0.125})O_3$				Experiments
		$\langle M \rangle$ (μ_B)	Gap (eV)	T_C (K)	$E_{formation}$ (eV atom^{-1})	$\langle M \rangle$ (μ_B)	Gap (eV)	T_C (K)	$E_{formation}$ (eV atom^{-1})	
	Sc	1.22	2.23	333	−2.90	0.61	2.32	508	−2.80	
	Ti	0.99	1.32	286	−2.91	0.49	1.17	492	−2.81	Ref. 40,53,54
	V	0.75	1.51	444	−2.84	0.61	0.12	349	−2.76	
	Cr	0.50	2.06	555	−2.84	0.25	2.28	523	−2.78	Ref. 49–52
3d	Mn	0.25	0.56	603	−2.71	0.13	0.98	540	−2.71	
atoms	Co	0.25	1.48	555	−2.64	0.12	1.45	698	−2.68	Ref. 59
doping	Ni	0.50	0.64	301	−2.59	0.49	0.40	492	−2.65	Ref. 48
	Cu	0.75	0.54	317	−2.53	0.37	0.65	528	−2.62	Ref. 56
	Zn	0.98	0.26	317	−2.61	0.49	0.00	413	−2.66	Ref. 27,55
	Y	1.23	1.98	301	−2.90	0.61	2.26	492	−2.80	
	Zr	0.98	1.23	254	−2.98	0.49	1.27	460	−2.84	
	Nb	0.75	1.65	174	−2.96	0.38	0.00	397	−2.82	
	Mo	0.55	0.62	365	−2.82	0.27	0.70	619	−2.76	Ref. 47
4d	Tc	0.28	1.13	380	−2.81	0.14	0.00	444	−2.75	
atoms	Ru	0.99	0.96	333	−2.72	0.49	1.07	524	−2.71	
doping	Rh	1.23	1.30	333	−2.69	0.61	1.60	540	−2.70	
	Pd	0.98	0.00	317	−2.57	0.49	0.56	528	−2.64	
	Ag	0.75	0.34	270	−2.48	0.37	0.57	476	−2.60	
	Cd	0.98	0.45	286	−2.56	0.49	0.00	413	−2.63	

The formation energy $E_{formation}$ of the host material $LaFeO_3$ is −2.71 eV atom^{-1}. Results here are obtained without Fe substrate.

where ε_{xx} and ε_{xy} are the diagonal and off-diagonal components of the dielectric tensor ε, ω is the frequency of incident light. The dielectric tensor ε can be obtained by the optical conductivity tensor σ as $\varepsilon(\omega) = \frac{4\pi i}{\omega}\sigma(\omega) + I$, where I is the unit tensor. The calculated $\varepsilon(\omega)$ as a function of photon energy for $LaFeO_3$, and $La(Fe_{0.75}D_{0.25})O_3$ with D = Ni, Cu, Zn, Mo, and Pd is shown in Fig. 5. The experimental result for Fe[88] and our DFT result for Fe bulk are also included for comparison. There are a big Kerr angle for $La(Fe_{0.75}D_{0.25})O_3$ with $\omega < 2$ eV, about 10 times bigger than bcc-Fe. It is worth noting that $LaFeO_3$ shows small but non-zero Kerr angle, despite its collinear AFM order, this may be related to the room temperature ferroelectricity of $LaFeO_3$[41]. Detailed results of the Kerr angle are given in Supplementary Fig. 9 in Supplementary Material.

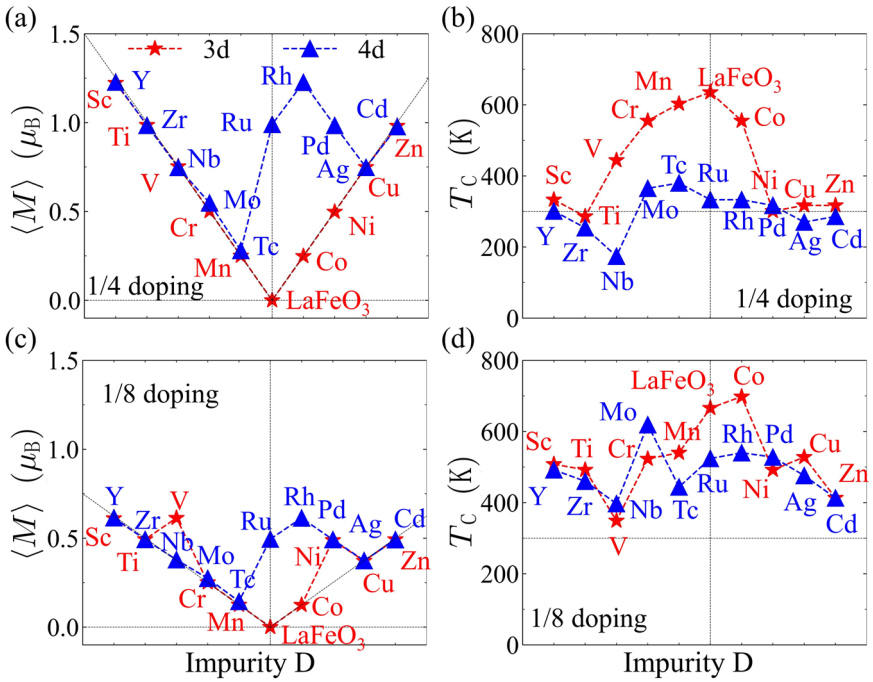

Fig. 4 | Average magnetic moment per magnetic atom $\langle M\rangle$ and Curie temperature T_C for $La(Fe_{0.75}D_{0.25})O_3$ and $La(Fe_{0.875}D_{0.125})O_3$. **a** Average magnetic moment per magnetic atom $\langle M\rangle$ and **b** Curie temperature T_C for $La(Fe_{0.75}D_{0.25})O_3$. **c** $\langle M\rangle$ and **d** T_C for $La(Fe_{0.875}D_{0.125})O_3$. The impurity D is taken as 3d and 4d transition metal elements. For comparison, the T_N = 650 K of host $LaFeO_3$ is also included in (**b**) and (**d**). Results here are obtained without Fe substrate.

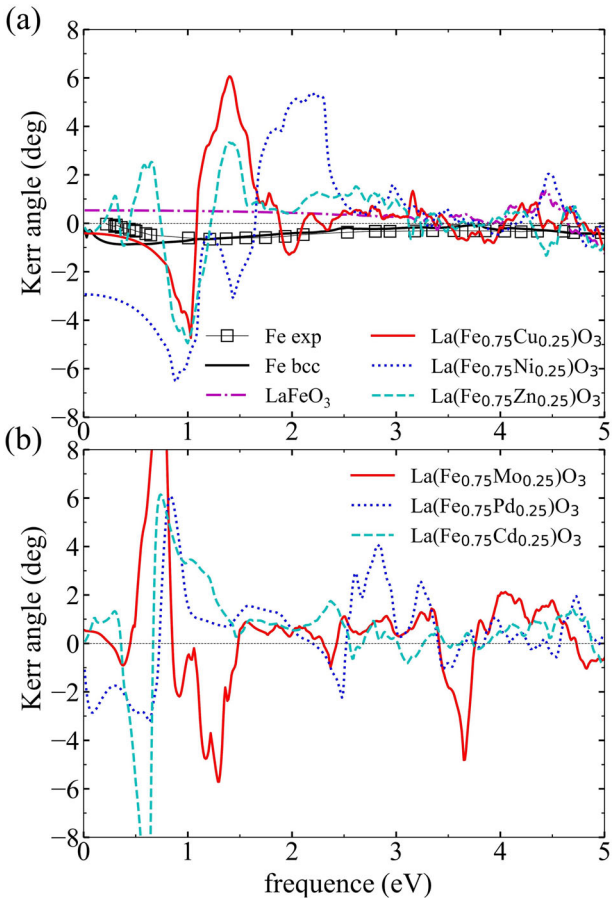

Fig. 5 | Results of magneto-optical Kerr rotation angle. **a** DFT results of Kerr angle for Fe, $LaFeO_3$ and $La(Fe_{0.75}D_{0.25})O_3$ with D = Ni, Cu, and Zn. **b** DFT results of Kerr rotation angle for $La(Fe_{0.75}D_{0.25})O_3$ with D = Mo, Pd, and Cd. Experimental Kerr rotation angle of Fe[88] is also included for comparison. Results here are obtained without Fe substrate.

Other high T_C FIM semiconductors

In addition to $LaFeO_3$, we also study the doping of other high T_N AFM insulators and semiconductors, including $BiFeO_3$, $SrTcO_3$, $CaTcO_3$. The calculation results are shown in Table 5. When 25% of the 3d transition metal element of the host are replaced by other 3d or 4d impurities, many room temperature FIM semiconductors are obtained in $LaFeO_3$, $BiFeO_3$, $SrTcO_3$, and $CaTcO_3$. All of these host materials are perovskite with T_N above 550 K and band gap bigger than 1.5 eV. Detailed results are given in Supplementary Figs. 4–8 and Supplementary Tables 4–6 in Supplemental Material. For the same impurity and concentration, T_C and band gap obtained after doping are positively related to T_N and band gap of AFM material. According to the calculation results, room temperature FIM semiconductors could be obtained by doping in AFM semiconductors, and a high T_N and a large band gap are needed.

Mean-field theory of the effect of doping on T_C

To study the influence of different impurities on T_C, as shown in Fig. 4, we use the Weiss molecular field approximate[89]. By the simple AFM Heisenberg model and the mean-field approximation (MFA), we get T_N of G-AFM $LaFeO_3$ as

$$T_N = 2\frac{J_0 S_0(S_0+1)}{k_B}, \tag{2}$$

where J_0 represents the nearest-neighbor coupling constant of Fe–Fe in $LaFeO_3$, S_0 is the magnetic moment of Fe in $LaFeO_3$, and k_B is the Boltzmann constant. By the help of DFT calculation, J_0 = 2.25 meV, S_0 = 4.15 μ_B. By Eq. (2), it has T_N = 1115 K. It is noted that the T_N = 1115 K by mean-field theory of Eq. (2) is much higher than the T_N = 650 K by the Monte Carlo simulation with the same J_0 and the T_N = 740 K of $LaFeO_3$ in experiment[26].

By the similar mean-field theory, we can obtain the expression of T_C for FIM semiconductors $La(Fe, D)O_3$. For simplicity, we only discuss the case of one impurity per unit cell without disorder, and only the nearest-neighbor coupling are considered.

The ratio of T_C and T_N is expressed as:

$$\begin{aligned}\frac{T_C}{T_N} &= t_0\sqrt{\frac{a+\sqrt{a^2-b}}{8}},\\ a &= \frac{1}{9}\left[6(6-z_{AB})t_D + z_{AB}z_{BA} + 6(6-z_{BA})\right],\\ b &= \frac{16}{9}t_D(6-z_{AB})(6-z_{BA}),\\ t_0 &= \frac{J_1}{J_0}\frac{S(S+1)}{S_0(S_0+1)}, t_D = \left(\frac{J_2}{J_1}\right)^2\frac{S_D(S_D+1)}{S(S+1)},\end{aligned} \quad (3)$$

where J_0, J_1 are the nearest-neighbor coupling constants of Fe–Fe in $LaFeO_3$ and La(Fe, D)O_3, respectively, J_2 is the nearest-neighbor coupling constants between Fe and D in La(Fe, D)O_3. S_0, S are the magnetic moments of Fe in $LaFeO_3$ and La(Fe, D)O_3, respectively, and S_D is the magnetic moment of D in La(Fe, D)O_3, z_{ij} is the coordination number of the site j near the site i. Supposing dopants at spin down sites, sublattice A mean Fe atoms spin up with nearest-neighbor impurities, sublattice B mean Fe atoms spin down without nearest-neighbor impurities, respectively. Here t_0 describes the ratio of Fe–Fe couplings in La(Fe, D)O_3 and $LaFeO_3$, t_D describes the ratio of Fe–D coupling and Fe–Fe coupling in La(Fe, D)O_3. See detailed information in Supplementary Sections 12 and 13 in Supplemental Material.

For case of 1/4 doping, the coordination number is $z_{AB} = 4$, $z_{BA} = 6$. For the case of 1/8 doping, the coordination number is $z_{AB} = 4$, $z_{BA} = 4$. Take these parameters and coupling constant and magnetic moment from DFT into Eq. (3), we obtain the ratio of T_C/T_N for $La(Fe_{0.75}D_{0.25})O_3$ and $La(Fe_{0.875}D_{0.125})O_3$, as shown in Fig. 6a, b, respectively. The ratio of T_C/T_N obtained by Eq. (3) with the mean-field approximation (MFA) and numerical calculations (DFT + MC) shown in Fig. 4 are in a good agreement. Thus, we note that it is possible to understand the effect of doping on T_C in FIM semiconductors La(Fe, D)O_3 by Eq. (3) of the conventional mean-field theory.

Table 5 | The calculated band gap and T_N for some high T_N AFM insulators and semiconductors with chemical formula ABO_3, and the calculated band gap, T_C and $\langle M\rangle$ for their doped materials $A(B_{0.75}D_{0.25})O_3$

Host ABO_3			$A(B_{0.75}D_{0.25})O_3$				Experiments
Material	Gap (eV)	T_N (K)	D	Gap (eV)	T_C (K)	$\langle M\rangle$ (μ_B)	Ref
$LaFeO_3$	2.4	650	V	1.51	444	0.75	
			Cr	2.06	555	0.50	49–52
			Co	1.48	555	0.25	59
			Mo	0.62	365	0.55	47
			Ru	0.96	333	0.99	
$BiFeO_3$	2.3	580	V	1.61	397	0.75	64
			Cr	1.96	524	0.50	64
			Co	2.00	476	0.25	61,62,64
			Mo	0.69	333	0.55	
			Ru	0.94	602	0.99	
$SrTcO_3$	1.5	883	V	0.84	793	0.47	
			Cr	0.00	634	0.25	
			Co	0.13	476	0.51	
			Mo	0.12	555	0.25	
			Ru	0.50	635	0.24	98
$CaTcO_3$	1.5	587	V	0.95	482	0.47	
			Cr	0.00	355	0.25	
			Co	0.14	343	0.51	
			Mo	0.09	393	0.25	
			Ru	0.56	444	0.24	

The impurity D is taken as some 3d and 4d transition metal elements. Results here are obtained without Fe substrate.

Discussion

Based on the DFT calculations, we show an approach to obtain room temperature FIM semiconductors by spin-dependent doping in high T_N insulators and semiconductors with large band gap. To demonstrate spin-dependent doping, the Mn-doped AFM insulator $LaFeO_3$ with FM sublattices bcc-Fe is studied by the DFT calculation. It is shown that the doped Mn impurities prefer to occupy one sublattice of $LaFeO_3$ due to the effective magnetic field of substrate bcc-Fe, and obtain the FIM semiconductor La(Fe, Mn)O_3 with large magnetic moment. By this method, we predict a series of room temperature FIM semiconductors in La(Fe, D)O_3, where D denoted the dopant of 3d and 4d transition metals. Large magneto-optical Kerr effect were found in $La(Fe_{0.75}D_{0.25})O_3$. By the equation of mean-field approximation, the ration of T_C in La(Fe, D)O_3 and T_N of $LaFeO_3$ are obtained, in a good agreement with the numerical results of DFT + MC. In the same way, the FIM semiconductors with high T_C are also predicted in some other high T_N AFM insulators and semiconductors, such as $BiFeO_3$, $SrTcO_3$, $CaTcO_3$, etc. Our results suggest that spin-dependent doping is a promising way to produce high T_C FIM semiconductors from high T_N AFM insulators and semiconductors.

Methods

Density functional theory calculations

Our calculations were based on the DFT as implemented in the Vienna ab initio simulation package (VASP)[90]. The exchange-correlation potential is described by the Perdew-Burke-Ernzerhof (PBE) form with the generalized gradient approximation (GGA)[91]. The electron-ion potential is described by the projector-augmented wave (PAW) method[92]. We carried out the calculation of GGA + U with U = 4 or 2 eV for 3d or 4d elements, respectively. The plane-wave cutoff energy is set to be 500 eV. The $4\times4\times1$, $4\times4\times3$, and $2\times4\times3$ Γ center k-point meshed were used for the Brillouin zone (BZ) sampling for supercells of $La(Fe_{0.75}D_{0.25})O_3$/bcc-Fe, $La(Fe_{0.75}D_{0.25})O_3$ and

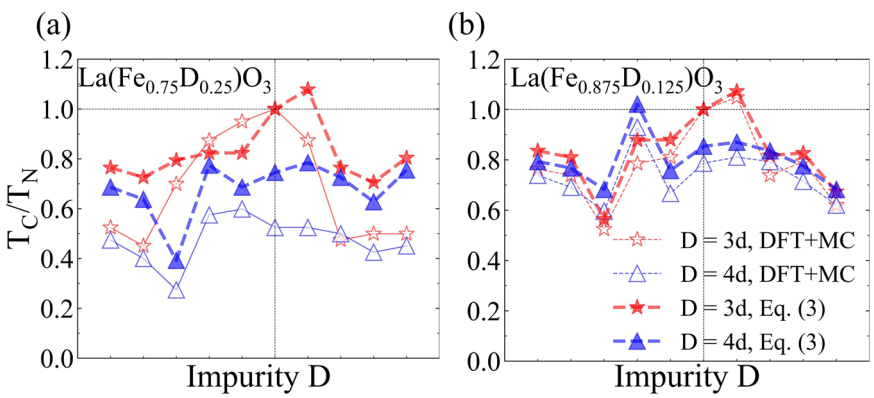

Fig. 6 | The ratio of T_C for $La(Fe_{1-x}D_x)O_3$ and T_N of $LaFeO_3$. For T_N of $LaFeO_3$ and T_C of $La(Fe_{1-x}D_x)O_3$, the ratio of T_C/T_N for **a** $x = 0.25$ and **b** $x = 0.125$. The impurity D is taken as 3d and 4d transition metal elements. The numerical results (DFT+MC) are taken from Fig. 4b, d. The mean-field approximation results are obtained by Eq. (3).

$La(Fe_{0.875}D_{0.125})O_3$, respectively. The structures of all materials were fully relaxed, where the convergence precision of energy and force were 10^{-6} eV and 10^{-2} eV $Å^{-1}$, respectively. The van der Waals effect is include with DFT-D3 method[93]. The Wannier90 code was used to construct a tight-binding Hamiltonian to calculate the Kerr rotation angle[94,95].

Monte Carlo program

The Heisenberg-type Monte Carlo simulation was performed on $10 \times 10 \times 10$ and $8 \times 8 \times 8$ lattice with 4000 and 4096 magnetic points for $La(Fe_{0.75}D_{0.25})O_3$ and $La(Fe_{0.875}D_{0.125})O_3$, respectively. More than 8×10^4 steps were carried for each temperature, and the last one-third steps were used to calculate the temperature-dependent physical quantities.

Data availability

The data supporting the findings of this paper are available from the corresponding authors upon reasonable request.

Code availability

The central code used in this paper is VASP. Detailed information related to the license and user guide are available at https://www.vasp.at.

Received: 1 October 2023; Accepted: 25 July 2024;
Published online: 03 September 2024

References

1. Huang, B. et al. Layer-dependent ferromagnetism in a van der Waals crystal down to the monolayer limit. *Nature* **546**, 270–273 (2017).
2. Lee, J. et al. Structural and optical properties of single- and few-layer magnetic semiconductor $CrPS_4$. *ACS Nano.* **11**, 10935–10944 (2017).
3. Cai, X. et al. Atomically thin $CrCl_3$: An in-plane layered antiferromagnetic insulator. *Nano. Lett.* **19**, 3993–3998 (2019).
4. Chu, J. et al. Sub-millimeter-scale growth of one-unit-cell-thick ferrimagnetic Cr_2S_3 nanosheets. *Nano. Lett.* **19**, 2154–2161 (2019).
5. Zhang, Z. et al. Direct photoluminescence probing of ferromagnetism in monolayer two-dimensional $CrBr_3$. *Nano. Lett.* **19**, 3138–3142 (2019).
6. Achinuq, B. et al. Covalent mixing in the 2D ferromagnet $CrSiTe_3$ evidenced by magnetic X-ray circular dichroism. *Phys. Status Solidi* **16**, 2100566 (2021).
7. Lee, K. et al. Magnetic order and symmetry in the 2D semiconductor CrSBr. *Nano. Lett.* **21**, 3511–3517 (2021).
8. Baltzer, P. K., Wojtowicz, P. J., Robbins, M. & Lopatin, E. Exchange interactions in ferromagnetic chromium chalcogenide spinels. *Phys. Rev.* **151**, 367–377 (1966).
9. Gong, C. et al. Discovery of intrinsic ferromagnetism in two-dimensional van der Waals crystals. *Nature* **546**, 265–269 (2017).
10. Ohno, H. Making nonmagnetic semiconductors ferromagnetic. *Science* **281**, 951–956 (1998).
11. Jungwirth, T., Sinova, J., Mašek, J., Kučera, J. & MacDonald, A. H. Theory of ferromagnetic (III, Mn)V semiconductors. *Rev. Mod. Phys.* **78**, 809–864 (2006).
12. Sato, K. et al. First-principles theory of dilute magnetic semiconductors. *Rev. Mod. Phys.* **82**, 1633–1690 (2010).
13. Dietl, T. & Ohno, H. Dilute ferromagnetic semiconductors: Physics and spintronic structures. *Rev. Mod. Phys.* **86**, 187–251 (2014).
14. Zhao, X. et al. $(Ba_{1-x}Na_x)F(Zn_{1-x}Mn_x)Sb$: A novel fluoride-antimonide magnetic semiconductor with decoupled charge and spin doping. *J. Semicond.* **43**, 112501 (2022).
15. Dong, J. et al. $(Ca, K)(Zn, Mn)_2As_2$: Ferromagnetic semiconductor induced by decoupled charge and spin doping in $CaZn_2As_2$. *J. Semicond.* **43**, 072501 (2022).
16. Huang, W., Lin, R., Chen, W., Wang, Y. & Zhang, H. High room-temperature magnetization in Co-doped TiO_2 nanoparticles promoted by vacuum annealing for different durations. *J. Semicond.* **42**, 072501 (2021).
17. Kalita, H., Bhushan, M. & Singh, L. R. A comprehensive review on theoretical concepts, types and applications of magnetic semiconductors. *Mater. Sci. Eng. B Solid-State Mater. Adv. Technol.* **288**, 116201 (2023).
18. Chen, L. et al. Enhancing the Curie temperature of ferromagnetic semiconductor (Ga, Mn)As to 200 K via nanostructure engineering. *Nano. Lett.* **11**, 2584–2589 (2011).
19. Zhao, K. et al. New diluted ferromagnetic semiconductor with Curie temperature up to 180 K and isostructural to the '122' iron-based superconductors. *Nat. Commun.* **4**, 1 (2013).
20. Zhao, K. et al. Ferromagnetism at 230 K in $(Ba_{0.7}K_{0.3})(Zn_{0.85}Mn_{0.15})_2As_2$ diluted magnetic semiconductor. *Chin. Sci. Bull.* **59**, 2524–2527 (2014).
21. Tu, N. T., Hai, P. N., Anh, L. D. & Tanaka, M. High-temperature ferromagnetism in heavily Fe-doped ferromagnetic semiconductor (Ga, Fe)Sb. *Appl. Phys. Lett.* **108**, 192401 (2016).
22. Tu, N. T., Hai, P. N., Anh, L. D. & Tanaka, M. Heavily Fe-doped ferromagnetic semiconductor (In, Fe)Sb with high Curie temperature and large magnetic anisotropy. *Appl. Phys. Express* **12**, 103004 (2019).
23. Wang, H. et al. High Curie temperature ferromagnetism and high hole mobility in tensile strained Mn-doped SiGe thin films. *Adv. Funct. Mater.* **30**, 2002513 (2020).
24. Marezio, M. & Dernier, P. The bond lengths in $LaFeO_3$. *Mater. Res. Bull.* **6**, 23–29 (1971).
25. Yakel, H. L. On the structures of some compounds of the perovskite type. *Acta. Crystallogr.* **8**, 394–398 (1955).
26. Koehler, W. & Wollan, E. Neutron-diffraction study of the magnetic properties of perovskite-like compounds $LaBO_3$. *J. Phys. Chem. Solids.* **2**, 100–106 (1957).
27. Manzoor, S. & Husain, S. Analysis of zn substitution on structure, optical absorption, magnetization, and high temperature specific heat anomaly of the nano-crystalline $LaFeO_3$. *J. Appl. Phys.* **124**, 065110 (2018).
28. Silva, J., Reyes, A., Esparza, H., Camacho, H. & Fuentes, L. $BiFeO_3$: A review on synthesis, doping and crystal structure. *Integr. Ferroelectr.* **126**, 47–59 (2011).
29. Rodriguez, E. E. et al. High temperature magnetic ordering in the 4d perovskite $SrTcO_3$. *Phys. Rev. Lett.* **106**, 067201 (2011).
30. Avdeev, M. et al. Antiferromagnetism in a technetium oxide. structure of $CaTcO_3$. *J. Am. Chem. Soc.* **133**, 1654–1657 (2011).
31. Sawatzky, G. A. & Allen, J. W. Magnitude and origin of the band gap in NiO. *Phys. Rev. Lett.* **53**, 2339–2342 (1984).
32. Marynowski, M., Franzen, W., El-Batanouny, M. & Staemmler, V. Observation of an extraordinary antiferromagnetic transition on the NiO (100) surface by metastable helium atom diffraction. *Phys. Rev. B* **60**, 6053–6067 (1999).
33. Yanagi, H. et al. Antiferromagnetic bipolar semiconductor lamnpo with ZrCuSiAs-type structure. *J. Appl. Phys.* **105**, 093916 (2009).
34. Beleanu, A. et al. Large resistivity change and phase transition in the antiferromagnetic semiconductors LiMnAs and LaOMnAs. *Phys. Rev. B* **88**, 184429 (2013).
35. Emery, N. et al. Giant magnetoresistance in oxypnictides (La, Nd) OMnAs. *Chem. Commun.* **46**, 6777 (2010).
36. Kriegner, D. et al. Multiple-stable anisotropic magnetoresistance memory in antiferromagnetic MnTe. *Nat. Commun.* **7**, 1 (2016).
37. Wijnheijmer, A. P. et al. Scanning tunneling microscopy reveals LiMnAs is a room temperature anti-ferromagnetic semiconductor. *Appl. Phys. Lett.* **100**, 112107 (2012).
38. Brockhouse, B. N. Antiferromagnetic structure in Cr_2O_3. *J. Chem. Phys.* **21**, 961–962 (1953).
39. Abdullah, M. M., Rajab, F. M. & Al-Abbas, S. M. Structural and optical characterization of Cr_2O_3 nanostructures: Evaluation of its dielectric properties. *AIP Adv.* **4**, 027121 (2014).
40. Sasikala, C. et al. Transition metal titanium (Ti) doped $LaFeO_3$ nanoparticles for enhanced optical structural and magnetic properties. *J. Alloy. Compd.* **712**, 870–877 (2017).

41. Acharya, S., Mondal, J., Ghosh, S., Roy, S. & Chakrabarti, P. Multiferroic behavior of lanthanum orthoferrite $LaFeO_3$. *Mater. Lett.* **64**, 415–418 (2010).
42. Takano, M., Kawachi, J., Nakanishi, N. & Takeda, Y. Valence state of the fe ions in $Sr_{1-y}La_yFeO_3$. *J. Solid. State. Chem.* **39**, 75–84 (1981).
43. Acharya, S., Deb, A., Das, D. & Chakrabarti, P. Enhanced magnetic behavior of Al substituted $LaFeO_3$ ($La_{1-x}Al_xFeO_3$, $x = 0.10$ and 0.30). *Mater. Lett.* **65**, 1280–1282 (2011).
44. Ahmed, M. A., Azab, A. A. & El-Khawas, E. H. Structural, magnetic and electrical properties of Bi doped $LaFeO_3$ nano-crystals, synthesized by auto-combustion method. *J. Mater. Sci. Mater.* **26**, 8765–8773 (2015).
45. Yao, Q. et al. Antiferromagnetic-ferromagnetic transition in Bi-doped $LaFeO_3$ nanocrystalline ceramics. *Ceram. Int.* **46**, 20472–20476 (2020).
46. Bidrawn, F., Lee, S., Vohs, J. M. & Gorte, R. J. The effect of Ca, Sr, and Ba doping on the ionic conductivity and cathode performance of $LaFeO_3$. *J. Electrochem. Soc.* **155**, B660 (2008).
47. Jana, S. et al. Charge disproportionate antiferromagnetism at the verge of the insulator-metal transition in doped $LaFeO_3$. *Phys. Rev. B* **99**, 075106 (2019).
48. Idrees, M. et al. Impedance spectroscopic investigation of delocalization effects of disorder induced by ni doping in $LaFeO_3$. *J. Phys. D Appl. Phys.* **44**, 105401 (2011).
49. Azad, A. et al. Structural and magnetic properties of $lafe_{0.5}Cr_{0.5}O_3$ studied by neutron diffraction, electron diffraction and magnetometry. *Mater. Res. Bull.* **40**, 1633–1644 (2005).
50. Rodrigues, A. et al. Positive exchange bias effect in $lacr_{0.5}Fe_{0.5}O_3$ perovskite. *J. Phys. Chem. Solids* **141**, 109334 (2020).
51. Xia, P., Mo, J., Chen, J., Liu, M. & Xia, Y. Magnetic properties and mössbauer study of perovskite $LaFeO_3$ and $LaFe_{0.5}Cr_{0.5}O_3$. *Phys. Status Solidi* **16**, 2200023 (2022).
52. Selvadurai, A. P. B. et al. Influence of Cr substitution on structural, magnetic and electrical conductivity spectra of $LaFeO_3$. *J. Alloy. Compd.* **646**, 924–931 (2015).
53. Phokha, S. et al. Structure, magnetic, and dielectric properties of Ti-doped $LaFeO_3$ ceramics synthesized by polymer pyrolysis method. *Mater. Res. Bull.* **67**, 118–125 (2015).
54. Sasikala, C. et al. Chemical, morphological, structural, optical, and magnetic properties of transition metal titanium Ti-doped $LaFeO_3$ nanoparticles. *J. Supercond. Nov. Magn.* **32**, 1791–1797 (2018).
55. Bhat, I., Husain, S., Khan, W. & Patil, S. Effect of Zn doping on structural, magnetic and dielectric properties of $LaFeO_3$ synthesized through sol-gel auto-combustion process. *Mater. Res. Bull.* **48**, 4506–4512 (2013).
56. Dogdibegovic, E. et al. Coupling between magnetic exchange and charge activation in Cu-doped $LaFeO_3$. *J. Am. Ceram. Soc.* **99**, 2035–2039 (2016).
57. Bhame, S. D., Joly, V. L. J. & Joy, P. A. Effect of disorder on the magnetic properties of $LaMn_{0.5}Fe_{0.5}O_3$. *Phys. Rev. B* **72**, 054426 (2005).
58. Triyono, D., Hanifah, U. & Laysandra, H. Structural and optical properties of Mg-substituted $LaFeO_3$ nanoparticles prepared by a sol-gel method. *Results Phys.* **16**, 102995 (2020).
59. Gu, J. et al. Synthesis of spindle-like co-doped $LaFeO_3$ porous microstructure for high performance n-butanol sensor. *Sens. Actuators B Chem.* **343**, 130125 (2021).
60. Troyanchuk, I. S. W. S. W. K. K. A. I. Crystal structure and spiral magnetic ordering of $BiFeO_3$ doped with manganese. *Appl. Phys. A* **74**, s1040–s1042 (2002).
61. Khajonrit, J., Wongpratat, U., Kidkhunthod, P., Pinitsoontorn, S. & Maensiri, S. Effects of Co doping on magnetic and electrochemical properties of $BiFeO_3$ nanoparticles. *J. Magn. Magn. Mater.* **449**, 423–434 (2018).
62. Sui, Y. et al. Enhancement of multiferroic in $BiFeO_3$ by Co doping. *J. Alloy. Compd.* **645**, 78–84 (2015).
63. Jun, Y.-K. et al. Effects of Nb-doping on electric and magnetic properties in multi-ferroic $BiFeO_3$ ceramics. *Solid State Commun.* **135**, 133–137 (2005).
64. Kharel, P. et al. Structural, magnetic, and electrical studies on polycrystalline transition-metal-doped $BiFeO_3$ thin films. *J. Phys. Condens. Matter* **21**, 036001 (2008).
65. Mukherjee, A., Basu, S., Chakraborty, G. & Pal, M. Effect of Y-doping on the electrical transport properties of nanocrystalline $BiFeO_3$. *J. Appl. Phys.* **112**, 014321 (2012).
66. Panigrahi, U. et al. Zn doping induced enhancement of multifunctional properties in NiO nanoparticles. *J. Alloy. Compd.* **833**, 155050 (2020).
67. Manna, S., Deb, A. K., Jagannath, J. & De, S. K. Synthesis and room temperature ferromagnetism in Fe doped NiO nanorods. *J. Phys. Chem.* **112**, 10659–10662 (2008).
68. Layek, S. & Verma, H. Room temperature ferromagnetism in Mn-doped NiO nanoparticles. *J. Magn. Magn. Mater.* **397**, 73–78 (2016).
69. Rahman, M. A., Radhakrishnan, R. & Gopalakrishnan, R. Structural, optical, magnetic and antibacterial properties of Nd doped NiO nanoparticles prepared by co-precipitation method. *J. Alloy. Compd.* **742**, 421–429 (2018).
70. Tariq, S., Ahmed, A. & Mubarak, A. A. Investigating the structural, mechanical, optical and magnetic attributes of $LaFe_{1-x}Cr_xO_3$ ferromagnetic materials by using DFT. *J. Comput. Electron.* **21**, 1202–1211 (2022).
71. Zhou, Y. et al. The electronic properties and structural stability of $LaFeO_3$ oxide by niobium doping: A density functional theory study. *Int. J. Hydrogen Energ.* **46**, 9193–9198 (2021).
72. Azouzi, W., Benabdallah, I., Sibari, A., Labrim, H. & Benaissa, M. Structural and optical properties of $LaFe_{1-x}V_xO_3$ as predicted by a DFT study. *Mater. Today Commun.* **26**, 101876 (2021).
73. Lu, S. et al. Tunable magnetism of 3d transition metal doped $BiFeO_3$. *J. Magn. Magn. Mater.* **439**, 57–66 (2017).
74. Rong, Q.-Y., Xiao, W.-Z., Xiao, G., Hu, A.-M. & Wang, L.-L. Magnetic properties in $BiFeO_3$ doped with Cu and Zn first-principles investigation. *J. Alloy. Compd.* **674**, 463–469 (2016).
75. Egbo, K. O., Ekuma, C. E., Liu, C. P. & Yu, K. M. Efficient p-type doping of sputter-deposited NiO thin films with Li, Ag, and Cu acceptors. *Phys. Rev. Mater.* **4**, 104603 (2020).
76. Dzyaloshinsky, I. A thermodynamic theory of "weak" ferromagnetism of antiferromagnetics. *J. Phys. Chem. Solids.* **4**, 241–255 (1958).
77. Scholl, A. et al. Observation of antiferromagnetic domains in epitaxial thin films. *Science* **287**, 1014–1016 (2000).
78. Seo, J. W. et al. Antiferromagnetic $LaFeO_3$ thin films and their effect on exchange bias. *J. Phys. Condens. Matter* **20**, 264014 (2008).
79. Folven, E. et al. Antiferromagnetic domain reconfiguration in embedded $LaFeO_3$ thin film nanostructures. *Nano Lett.* **10**, 4578–4583 (2010).
80. Hallsteinsen, I. et al. Magnetic domain configuration of (111)-oriented $LaFeO_3$ epitaxial thin films. *APL Mater.* **5**, 086107 (2017).
81. Gao, R. et al. Oxygen defects-engineered $LaFeO_{3-x}$ nanosheets as efficient electrocatalysts for lithium-oxygen battery. *J. Catal.* **384**, 199–207 (2020).
82. Yu, J. et al. Ag-modified porous perovskite-type $LaFeO_3$ for efficient ethanol detection. *Nanomaterials* **12**, 1768 (2022).
83. Li, Y. et al. Structure and magnetic properties of Cr-doped ZnO nanoparticles prepared under high magnetic field. *Solid State Commun.* **150**, 751–754 (2010).
84. Yuan, L.-D., Wang, Z., Luo, J.-W., Rashba, E. I. & Zunger, A. Giant momentum-dependent spin splitting in centrosymmetric low-Z antiferromagnets. *Phys. Rev. B* **102**, 014422 (2020).

85. Yuan, L.-D., Wang, Z., Luo, J.-W. & Zunger, A. Prediction of low-Z collinear and noncollinear antiferromagnetic compounds having momentum-dependent spin splitting even without spin-orbit coupling. *Phys. Rev. Mater.* **5**, 014409 (2021).
86. Yuan, L.-D., Zhang, X., Acosta, C. M. & Zunger, A. Uncovering spin-orbit coupling-independent hidden spin polarization of energy bands in antiferromagnets. *Nat. Commun.* **14**, 5301 (2023).
87. Okugawa, T., Ohno, K., Noda, Y. & Nakamura, S. Weakly spin-dependent band structures of antiferromagnetic perovskite $LaMO_3$(M = Cr, Mn, Fe). *J. Phys. Condens. Matter* **30**, 075502 (2018).
88. Oppeneer, P. M., Maurer, T., Sticht, J. & Kübler, J. Ab initio calculated magneto-optical Kerr effect of ferromagnetic metals: Fe and Ni. *Phys. Rev. B* **45**, 10924–10933 (1992).
89. Dai, D. S. & Qian, K. M. *Ferromagnetism*, Vol. 1 (Science Press, Beijing, 2017).
90. Kresse, G. & Furthmüller, J. Efficient iterative schemes for ab initio total-energy calculations using a plane-wave basis set. *Phys. Rev. B* **54**, 11169–11186 (1996).
91. Perdew, J. P., Burke, K. & Ernzerhof, M. Generalized gradient approximation made simple. *Phys. Rev. Lett.* **77**, 3865–3868 (1996).
92. Blöchl, P. E. Projector augmented-wave method. *Phys. Rev. B* **50**, 17953–17979 (1994).
93. Grimme, S., Antony, J., Ehrlich, S. & Krieg, H. A consistent and accurate ab initio parametrization of density functional dispersion correction (DFT-D) for the 94 elements H-Pu. *J. Chem. Phys.* **132**, 154104 (2010).
94. Mostofi, A. A. et al. Wannier90: A tool for obtaining maximally-localised Wannier functions. *Comput. Phys. Commun.* **178**, 685–699 (2008).
95. Mostofi, A. A. et al. An updated version of wannier90: A tool for obtaining maximally-localised Wannier functions. *Comput. Phys. Commun.* **185**, 2309–2310 (2014).
96. Ren, Y. et al. Enhanced thermoelectric performance of MnTe via Cu doping with optimized carrier concentration. *J. Materiomics* **2**, 172 (2016).
97. Polash, M. M. H., Rasoulianboroujeni, M. & Vashaee, D. Magnon and spin transition contribution in heat capacity of ferromagnetic Cr-doped MnTe: Experimental evidence for a paramagnetic spin-caloritronic effect. *Appl. Phys. Lett.* **117**, 043903 (2020).
98. Reynolds, E. M. et al. Magneto-structural coupling in $SrTc_xRu_{1-x}O_3$ (x = 0.25, 0.5) perovskites. *J. Solid. State. Chem.* **287**, 121378 (2020).

Acknowledgements

This work is supported by the National Key R&D Program of China (Grant No. 2022YFA1405100), National Natural Science Foundation of China (Grant No. 12074378), and Chinese Academy of Sciences (Grants No. YSBR-030, No. JZHKYPT-2021-08, No. XDB33000000).

Author contributions

J.W.L. and B.G. conceived the original ideas and supervised the work. J.W.L. performed the first principles calculations and data analysis. G.S. joined the data discussions. All authors participated in discussing and editing the manuscripts.

Competing interests

The authors declare no competing interests.

Additional information

Supplementary information The online version contains supplementary material available at https://doi.org/10.1038/s41524-024-01362-y.

Correspondence and requests for materials should be addressed to Gang Su or Bo Gu.